Jupiter's atmospheric jet-streams extend thousands of kilometers deep

Y. Kaspi[1*], E. Galanti[1], W. B. Hubbard[2], D. J. Stevenson[3], S. J. Bolton[4], L. Iess[5], T. Guillot[6], J. Bloxham[7], J. E. P. Connerney[8], H. Cao[7], D. Durante[5], W. M. Folkner[9], R. Helled[10], A. P. Ingersoll[3], S. M. Levin[9], J. I. Lunine[11], Y. Miguel[6], B. Militzer[12], M. Parisi[9], and S. M. Wahl[12]

[1] *Weizmann Institute of Science, Rehovot, 76100, Israel*

[2] *University of Arizona, Tucson, AZ, 85721, USA*

[3] *California Institute of Technology, Pasadena, CA, 91125, USA*

[4] *Southwest Research Institute, San Antonio, Texas, USA*

[5] *Sapienza Universita di Roma, 00184, Rome, Italy*

[6] *Université Côte d'Azur, OCA, Lagrange CNRS, 06304, Nice, France*

[7] *Harvard University, Cambridge, MA, 02138, USA*

[8] *NASA/GSFC, Greenbelt, Maryland, 20771, USA*

[9] *Jet Propulsion Laboratory, California Institute of Technology, Pasadena, CA, 91109, USA*

[10] *University of Zurich, 8057, Zurich, Switzerland*

[11] *Cornell University, Ithaca, NY, 14853, USA*

[12] *University of California, Berkeley, CA, 94720, USA*

The depth to which Jupiter's observed east-west jet-streams extend has been a long-standing question[1,2]. Resolving this puzzle has been a primary goal of NASA's Juno mission to Jupiter[3,4], which has been in orbit around the gas giant since July 2016. Juno's gravitational measure-

1

ments have revealed that Jupiter's gravitational field is north-south asymmetric[5], which is a signature of atmospheric and interior flows within the planet[6]. Here we report that the measured gravitational harmonics J_3, J_5, J_7 and J_9 indicate that the observed jet-streams, as they appear at the cloud-level, extend down to depths of thousands of kilometers beneath the cloud-level, likely to the region of magnetic dissipation at a depth of about 3000 km[7,8]. Inverting the measured gravity values into a wind field[9], we provide the most likely vertical profile of the deep atmospheric and interior flow, and the latitudinal dependence of its depth. Furthermore, the even gravity harmonics J_8 and J_{10} resulting from this flow profile match the measurement as well, when taking into account the contribution of the interior structure[10]. These results indicate that the mass of the dynamical atmosphere is about one percent of Jupiter's total mass.

The Juno gravity measurements to date have improved the accuracy of the known gravity harmonics J_2, J_4, J_6 and J_8 by more than two orders of magnitude[5,12]. These low-degree even gravity harmonics are mostly affected by Jupiter's interior density structure and its shape[13], and therefore, although the signal from these harmonics may contain a contribution from the flow (ΔJ_n)[14], it is difficult to use these harmonics to directly infer information about the flows. The gravity measurements also revealed north-south asymmetries in the gravity field of Jupiter[5], resulting in considerable values of the odd gravity harmonics J_3, J_5, J_7 and J_9 (see Table 1). Since a gas planet rotating as a solid-body has no asymmetry between north and south, any non-zero value of the odd J_n must come from dynamics[6]. As the observed cloud-level flow is not hemispherically symmetric (Fig. 1), if enough mass is involved in the asymmetric component of the flow, this will

2

42 manifest large odd J_n. At present, the gravity harmonics beyond J_{10} are still beneath the level of

43 the measurement uncertainty[5], and because the low-degree even J_n are dominated by solid-body

44 rotation, the only current measurements that can be uniquely related to the dynamics are the low-

45 degree odd harmonics J_3 to J_9. Therefore, in the current study, we use only those to infer the depth

46 of the cloud-level winds.

47 Since Jupiter is rotating at a short period of 9.92 hours, the flow within the planet to lead-

48 ing order is in geostrophic balance, meaning the momentum budget is dominated by the balance

49 between the Coriolis force and the horizontal pressure gradients. As a consequence, the flow to

50 leading order is in thermal wind balance, namely,

$$2\Omega \cdot \nabla \left(\rho_s \mathbf{u} \right) = \nabla \rho' \times \mathbf{g}, \tag{1}$$

51 where Ω is the rotation rate of the planet, $\mathbf{u}$ is the velocity field, ρ_s and ρ' are the static and dy-

52 namic components of density, respectively, and $\mathbf{g}$ is the gravity obtained by integrating ρ_s (see

53 Methods)[15] . Non-spherical effects can play a role in this balance (e.g., the deviation of $\mathbf{g}$ from

54 radial symmetry)[16,17]; however, it has been shown that to leading order Eq. (1) captures well the

55 dynamical balance[17,18] (Fig. ED1). As the gravity harmonics induced by the flow are directly re-

56 lated to ρ', this enables to relate the flow field and the gravity spectrum. Thus, given the measured

57 gravitational field, inversion of Eq. (1) allows to infer the flow profile that best matches the mea-

58 surement. For this inversion we use an optimization based on the adjoint method[9] (see Methods).

59 The relation between the odd gravity harmonics and the flow is shown in Fig. 2 for a simple

60 model[6] where the depth of the cloud-level wind is parametrized with a single decay parameter,

H. In this scenario, the interior flow is an extension of the cloud-level flow, along the direction of the spin axis due to angular momentum constraints (see below)[15,19], but decays exponentially in radius with H being the e-folding decay depth[6,20]. The Juno measured values (Fig. 2, dashed), show that for all four harmonics, independently, the theoretical values capture the correct sign of the measured harmonics and indicate that the e-folding decay depth of the flow is between 1000 and 3000 km (Fig. 2, gray shading). Inverting the gravity field[9], taking into consideration the uncertainties of each of the measured harmonics and their cross-correlated uncertainties (the error covariance matrix, see Methods), gives an e-folding decay depth of ~ 1500 km. Note however that the measured value of J_5 deviates by about a factor of two from the corresponding theoretical value of a single parameter deep wind profile, suggesting that a more elaborate vertical flow profile than the simple exponential decay is needed in order to match the data.

Given that the measurements provide four non-zero odd gravity harmonics, indeed a more complex optimization of the vertical and meridional flow profile is feasible. Motivated by the Galileo probe measurement of a relatively constant wind profile between 4 and 22 bars[21], and magnetohydrodynamic theory suggesting that Ohmic dissipation will cause a more abrupt decay of the flow at depth[7,8,22,23] we add in addition to the exponential decay function used in the first estimation (Fig. 2), a vertical decay profile expressed as a hyperbolic tangent function and a free parameter, α, representing the ratio between the two functions. This allows for a much wider range of vertical decay profiles, with three free parameters defining the vertical profile of the flow: the depth H representing the inflection point of the $\tanh$ function, ΔH representing the decay width of the $\tanh$ function and the ratio α between the $\tanh$ and an exponential decay with the same

4

82 decay depth H. Using these three parameters as control parameters in the inverse adjoint model,

83 the optimization process (Fig. 3) minimizes a cost-function taking into account the uncertain-

84 ties in the gravity measurements, including the error covariance between the different harmonics

85 (Methods)[9,24].

86   Beginning with an assumed vertical decay profile as an initial condition (Fig. 3a, dashed line,

87 and black squares in Fig. 3b,c), the optimization iteratively minimizes the cost-function reaching

88 a unique global minimum in the three dimensional parameter space of H, ΔH and α (red dot,

89 Fig. 3b,c). The best optimized solution, defining a particular vertical profile of the zonal flow (red

90 line, Fig. 3a), is achieved with $H = 1803 \pm 351$ km, $\Delta H = 1570 \pm 422$ km and $\alpha = 0.92 \pm 0.26$,

91 where the error is calculated by the optimization process (see Methods), indicating a very deep

92 flow profile containing a significant mass. Note that the minimum of the cost-function for ΔH

93 is rather flat towards lower ΔH (Fig. 3b), indicating that a flow profile with a much more abrupt

94 decay at depth is compatible with the measured J_n. Integrating the density profile ρ_s down to

95 where the flow decreases significantly (~ 3000 km) reveals that this region contains about 1%

96 of Jupiter's mass (the mass dependence on depth is shown in Fig. ED2). This large mass of the

97 dynamical atmosphere (the region that is differentially rotating) is consistent with the observed

98 jets' persistence over the past several decades[2]. In a companion paper we show, based on the even

99 harmonics, that beneath this dynamical atmosphere, in Jupiter's deep interior, there is likely very

100 little flow[10]. In terms of angular momentum, the angular momentum of this flow is 2×10^{-5} that

101 of the solid-body planet.

5

102   The solution shown in Fig. 3a (red line) implies that the meridional profile of the flow at depth

103   is strongly correlated to the cloud-level flow. To test the statistical significance of this solution we

104   generate a large set of synthetic latitudinal wind profiles (Fig. ED3), by expanding the observed

105   flow up to high degree Legendre polynomials and summing them back up while assigning random

106   signs to the expansion coefficients. We find that the solution using the observed cloud-level wind

107   profile (Fig. ED4, black) is one of the closest solutions to the measurements (Fig. ED4, red) and

108   only a small subset of the random flow profiles (less than 1%) give a lower cost-function value

109   (Fig. ED4, green). This shows that it is statistically improbable that the meridional profile of

110   the flow changes with depth, or that the solution was found by chance (see further discussion in

111   Methods).

112   Considering the angular momentum budget is helpful for developing a mechanistic under-

113   standing of these deep dynamics. Modeling studies have suggested[19,22], that the leading order

114   angular momentum balance is $\mathbf{u} \cdot \nabla M = D - S$, where $\mathbf{u}$ is the mass averaged velocity, D is

115   the drag due to the Lorentz force at depth and $S = \frac{1}{\rho} \nabla \cdot \left(\rho \overline{\mathbf{u}'M'} \right)$ is the eddy angular momen-

116   tum flux divergence, with the bar indicating a zonal and time mean. At the observed cloud-level

117   the eastward (westward) jets are correlated with regions of eddy momentum flux convergence (di-

118   vergence), i.e., where S is negative (positive)[22,25]. Below that, where the eddy momentum flux

119   convergence is expected to become weak[25], i.e., $\mathbf{u} \cdot \nabla M \approx 0$, the flow is along angular momen-

120   tum surfaces, which on Jupiter are almost entirely parallel to the axis of rotation[15,19,26]. Then,

121   in the deep region, where the fluid becomes electrically conducting (mainly due to pressure ion-

122   ization) and the Lorentz force may become important (depending on the magnetic field structure)

6

the leading order balance is $\mathbf{u} \cdot \nabla M = D$ and the circulation closes. Kinematic dynamo models,

calculating the magnetic drag at depth based on the radially varying electric conductivity inside

Jupiter, find that the depth where the Lorentz drag (D) becomes important is ~ 3000 km[7,8]. Thus,

the theoretical magnetic field considerations and the gravity measurements, which are completely

independent, give very consistent results.

Three-dimensional hydrodynamic models of Jupiter, driven by shallow atmospheric turbulence[22,27]

or deep internal convection[15], have found that the low latitudes are often more barotropic than high

latitudes. Thus, an additional complexity that can be added to the optimization is allowing the de-

cay depth (H) to vary with latitude. In order to limit the number of optimized parameters the decay

depth is expanded in Legendre polynomials to second order, increasing the number of optimized

parameters to four (see Methods). Similar to the case of a latitudinally independent verical profile

(Fig. 3), in this case the optimized vertical decay profile is rather barotropic at lower depths and ex-

tends very deep (Fig. 4a). The optimization uncertainty is shown graphically by the blue shading,

with the values for the profile at the equator are given in the caption. At higher latitudes, the verti-

cal decay occurs at shallower depths, and the associated uncertainty grows to ~ 500 km (Fig. 4b).

The values of J_n corresponding to the solutions of Figs. 3 and 4 appear in Table 1. Note that

with more free parameters than used in these optimizations, closer matches to the measurements

can be reached. However, the power of these solutions is that they are based on relatively simple

extensions of the cloud-level flow, giving results remarkably close to all four independent gravity

measurements, and regardless of the exact vertical profile indicate that the observed cloud-level

flows extend to depths of thousands of kilometers.

7

144   The flow profile determined by the odd harmonics has also a signature in the even harmonics.

145   Due to the uncertainty in the bulk interior density structure of Jupiter[10,28], there is a wide range

146   of solutions for the static gravity harmonics (J_n^s) for the lowest harmonics[14,28], which does not

147   allow testing uniquely whether the ΔJ_n from the even harmonics matches the measured values via

148    $\Delta J_n = J_n - J_n^s$. However, for J_8 and J_{10} the interior models are very constraining[10], giving values

149   between -245.7×10^{-8} and -246.3×10^{-8} for J_8^s, and between 20.1×10^{-8} and 20.4×10^{-8} for J_{10}^s

150   (for interior models that match also J_4 and J_6). The measured Juno values are $J_8 = -242.6 \pm 0.8 \times$

151   10^{-8} and $J_{10} = 17.2 \pm 2.3 \times 10^{-8}$, meaning that a positive (negative) correction by the dynamics

152   is needed in order to match the measurements for J_8 (J_{10}). The values corresponding to the flow

153   profiles presented in Figs. 3 and 4 (Table ED1) are indeed such that for both cases, and for both

154   J_8 and J_{10}, the dynamical corrections can reconcile the differences between the measurements and

155   the internal models, further confirming that the inferred flow profile presented here matches the

156   measurements from Juno. In a companion paper it is shown that using the range of current interior

157   models gives further constraints on possible deeper interior flow[10].

158   Juno's gravity measurements are consistent with Juno's microwave radiometer measurements

159   indicating a north-south asymmetry in the sub cloud-level atmospheric composition, and a di-

160   rect signature of the main equatorial belt to the maximum depth of the microwave sensitivity at

161   ~ 1000 bars[12,29]. With more Juno orbits the microwave measurements[4,30] will obtain greater and

162   improved thermal mapping of the deep atmosphere, which will better constrain the water and am-

163   monia abundances as well as the atmospheric flows at those levels. As the Juno mission completes

164   its global mapping of Jupiter, the combination of the gravity, magnetic and microwave data may

provide further insights into the coupling between Jupiter's deep interior and atmospheric flows.

1. Dowling, T. E. Dynamics of Jovian atmospheres. *Ann. Rev. Fluid Mech.* **27**, 293–334 (1995).

2. Vasavada, A. R. & Showman, A. P. Jovian atmospheric dynamics: An update after Galileo and Cassini. *Reports of Progress in Physics* **68**, 1935–1996 (2005).

3. Hubbard, W. B. Note: Gravitational signature of Jupiter's deep zonal flows. *Icarus* **137**, 357–359 (1999).

4. Bolton, S. J. Juno final concept study report. Tech. Rep. AO-03-OSS-03, New Frontiers, NASA (2005).

5. Iess, L. *et al.* Jupiter's asymmetric gravity field. *Nature* (2018). In press, this issue.

6. Kaspi, Y. Inferring the depth of the zonal jets on Jupiter and Saturn from odd gravity harmonics. *Geophys. Res. Lett.* **40**, 676–680 (2013).

7. Liu, J., Goldreich, P. M. & Stevenson, D. J. Constraints on deep-seated zonal winds inside Jupiter and Saturn. *Icarus* **196**, 653–664 (2008).

8. Cao, H. & Stevenson, D. J. Zonal flow magnetic field interaction in the semi-conducting region of giant planets. *Icarus* **296**, 59–72 (2017).

9. Galanti, E. & Kaspi, Y. An adjoint based method for the inversion of the Juno and Cassini gravity measurements into wind fields. *Astrophys. J.* **820**, 91 (2016).

10. Guillot, T. *et al.* Constraints on deep differential rotation in Jupiter's interior. *Nature* (2018). In press, this issue.

11. Tollefson, J. *et al.* Changes in Jupiter's zonal wind profile preceding and during the Juno mission. *Icarus* **296**, 163–178 (2017).

12. Bolton, S. J. *et al.* Jupiter's interior and deep atmosphere: The initial pole-to-pole passes with the Juno spacecraft. *Science* **356**, 821–825 (2017).

13. Hubbard, W. B. High-precision Maclaurin-based models of rotating liquid planets. *Astrophys. J. Let.* **756**, L15 (2012).

14. Kaspi, Y. *et al.* The effect of differential rotation on Jupiter's low-degree even gravity moments. *Geophys. Res. Lett.* **44**, 5960–5968 (2017).

15. Kaspi, Y., Flierl, G. R. & Showman, A. P. The deep wind structure of the giant planets: Results from an anelastic general circulation model. *Icarus* **202**, 525–542 (2009).

16. Zhang, K., Kong, D. & Schubert, G. Thermal-gravitational wind equation for the wind-induced gravitational signature of giant gaseous planets: Mathematical derivation, numerical method and illustrative solutions. *Astrophys. J.* **806**, 270–279 (2015).

17. Cao, H. & Stevenson, D. J. Gravity and zonal flows of giant planets: From the Euler equation to the thermal wind equation. *J. Geophys. Res. (Planets)* **122**, 686–700 (2017).

18. Galanti, E., Kaspi, Y. & Tziperman, E. A full, self-consistent, treatment of thermal wind balance on fluid planets. *J. Fluid Mech.* **810**, 175–195 (2017).

19. Schneider, T. & Liu, J. Formation of jets and equatorial superrotation on Jupiter. *J. Atmos. Sci.* **66**, 579–601 (2009).

20. Kaspi, Y., Hubbard, W. B., Showman, A. P. & Flierl, G. R. Gravitational signature of Jupiter's internal dynamics. *Geophys. Res. Lett.* **37**, L01204 (2010).

21. Atkinson, D. H., Pollack, J. B. & Seiff, A. The Galileo probe doppler wind experiment: Measurement of the deep zonal winds on Jupiter. *J. Geophys. Res.* **103**, 22911–22928 (1998).

22. Liu, J. & Schneider, T. Mechanisms of jet formation on the giant planets. *J. Atmos. Sci.* **67**, 3652–3672 (2010).

23. Liu, J., Schneider, T. & Kaspi, Y. Predictions of thermal and gravitational signals of Jupiter's deep zonal winds. *Icarus* **224**, 114–125 (2013).

24. Galanti, E. & Kaspi, Y. Deciphering Jupiters deep flow dynamics using the upcoming Juno gravity measurements and an adjoint based dynamical model. *Icarus* **286**, 46–55 (2017).

25. Salyk, C., Ingersoll, A. P., Lorre, J., Vasavada, A. & Del Genio, A. D. Interaction between eddies and mean flow in Jupiter's atmosphere: Analysis of Cassini imaging data. *Icarus* **185**, 430–442 (2006).

26. Busse, F. H. A simple model of convection in the Jovian atmosphere. *Icarus* **29**, 255–260 (1976).

27. Lian, Y. & Showman, A. P. Generation of equatorial jets by large-scale latent heating on the giant planets. *Icarus* **207**, 373–393 (2010).

11

28. Wahl, S. *et al.* Comparing Jupiter interior structure models to Juno gravity measurements and the role of an expanded core. *Geophys. Res. Lett.* **44**, 4649–4659 (2017).

29. Li, C. *et al.* The distribution of ammonia on Jupiter from a preliminary inversion of Juno microwave radiometer data. *Geophys. Res. Lett.* **44**, 5317–5325 (2017).

30. Janssen, M. A. *et al.* Microwave remote sensing of Jupiter's atmosphere from an orbiting spacecraft. *Icarus* **173**, 447–453 (2005).

Author contributions   Y.K. and E.G. designed the study. Y.K. wrote the paper. E.G. developed the gravity inversion model. D.J.S. led the working group within the Juno Science Team and provided theoretical support. W.B.H. initiated the Juno gravity experiment and provided theoretical support. W.B.H, T.G., Y.M, R.H., B.M. and S.L.W. provided interior models and tested the implications of the results. L.I., D.D, W.M.F. and M.P. carried out the analysis of the Juno gravity data. H.C., D.J.S. and J.B. supported the interpretation with regards to the magnetic field. J.I.L and A.P.I provided theoretical support. S.J.B., S.M.L. and J.E.P.C.

242 supervised the planning, execution, and definition of the Juno gravity experiment. All authors contributed

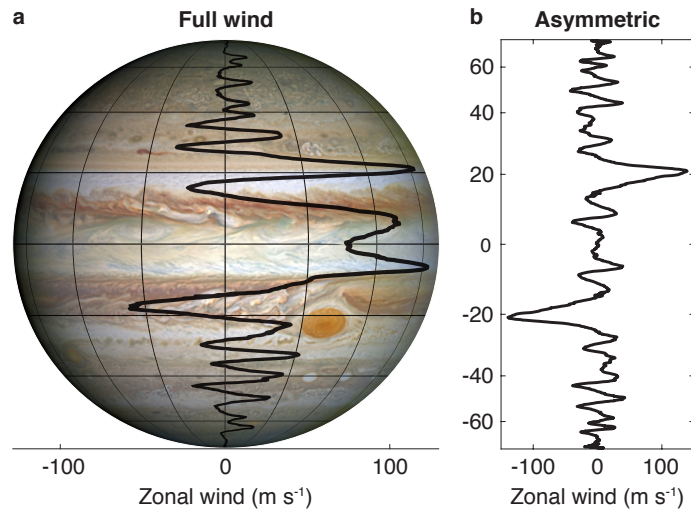243 to the discussion and interpretation of the results within the Juno Interiors Working Group.

Figure 1: **Jupiter's asymmetric zonal velocity field. a.** An image of Jupiter taken by the Hubble wide field camera in 2014, with the cloud-level zonal flows (thick black line) as function of latitude as measured during Juno's 3rd perijove of Jupiter on December 11th 2016[11]. Grid latitudes are as in panel (b) and the longitudinal spread is $45°$. Zonal flow scale is the same as the longitudinal grid on the sphere. **b.** The asymmetric component of the flow is taken as the difference between the northern and southern hemisphere cloud-level flows.
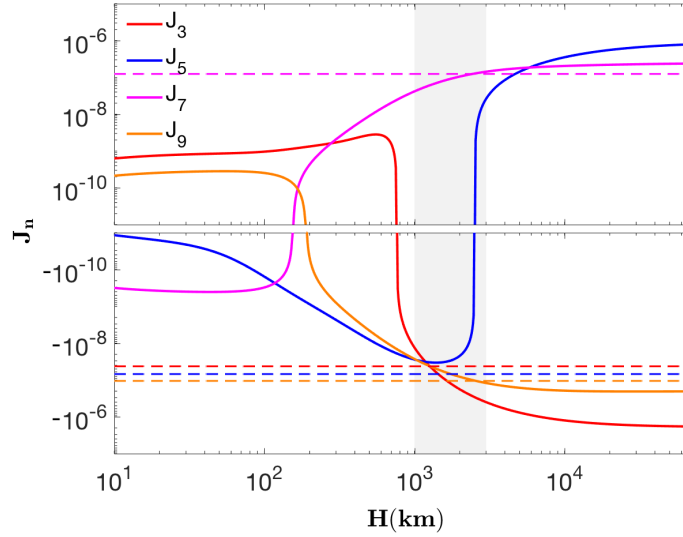
Figure 2: **The odd gravity harmonics as function of a single e-folding decay depth parameter**
H. Theoretical predicted values[6] (soild) and the Juno measured values[5] (dashed, corresponding to
the values in Table 1) for J_3 (red), J_5 (blue), J_7 (magenta) and J_9 (orange) are shown as function
of H. All four gravity harmonic measurements, independently, indicate the e-folding depth of the
flow is 1000-3000 km (gray shading). All four odd harmonics are small if the flows are shallow,
and become large for deeper flows that contain more mass. The change in sign at different decay
depths depends on the way the flow pattern projects onto the different Legendre polynomials.
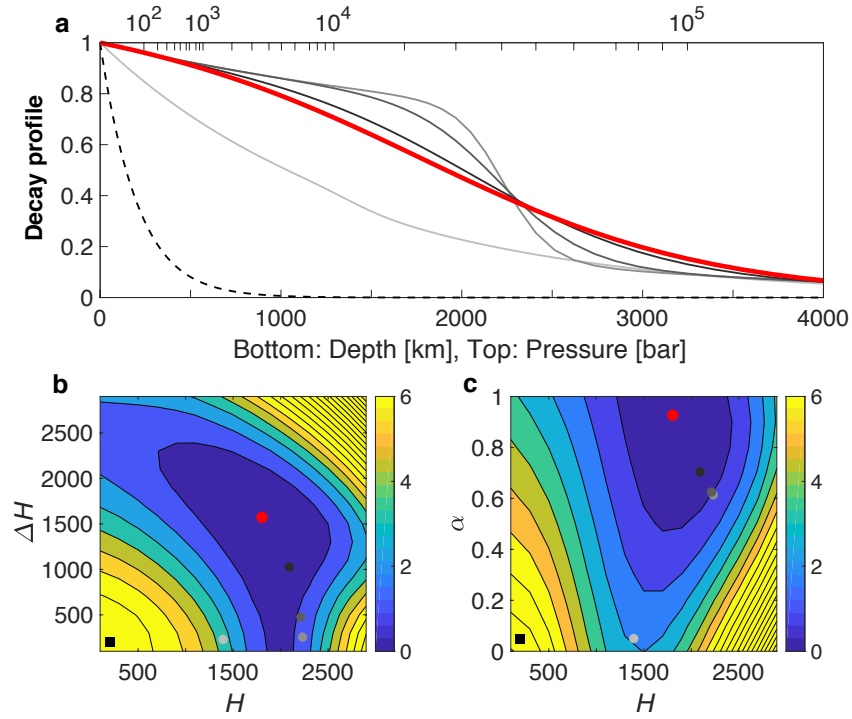
Figure 3: **Jupiter's optimized vertical wind profile. a.** The vertical profile of the flow from the optimization process, beginning with an initial profile (dashed), which evolves along the optimization process (from light to dark shades of gray) leading to the best optimized vertical profile (red), with the parameters: $H = 1803 \pm 351$ km, $\Delta H = 1570 \pm 422$ km and $\alpha = 0.92 \pm 0.26$ (Eq. M13 in Methods). Abscissa shows both the depth (bottom) and pressure (top) beneath the 1 bar level. **b.** The cost-function in the plane of H and ΔH showing a robust minimum at $H = 1803$ km and $\Delta H = 1570$ km (red dot). **c.** The cost-function in the plane of H and α showing a minimum at $H = 1803$ km and $\alpha = 0.92$ (red dot). In both panels b and c the gray shaded dots correspond to the gray shaded curves in panel a. Cost-function values in the color-bar are divided by 1000 (see calculation in Methods). A statistical significance test for the latitudinal dependence of the flow profile appears in Figs. ED4 and ED5 (Methods).
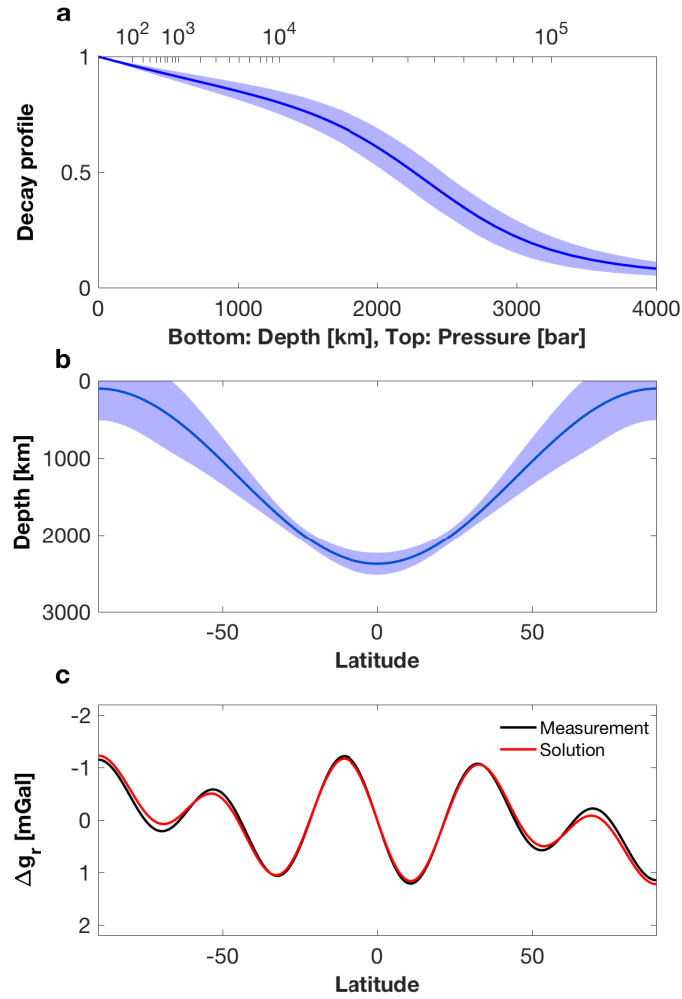
Figure 4: **Jupiter's optimized vertical wind profile when allowing for its latitudinal variation.**
a. The vertical profile of the flow at the equator from the optimization process (blue line) and its uncertainty (blue shading). Best optimized values at the equator are $H = 2379 \pm 142$, $\Delta H = 819 \pm 437$ and $\alpha = 0.62 \pm 0.09$. Abscissa shows both the depth (bottom) and pressure (top) beneath the 1 bar level. **b.** The variation of the inflection point (as shown in panel a) with latitude (blue line) and its uncertainty (blue shading). Details of the latitudinal dependence of H and its functional form are given in Methods (Eq. M13). **c.** The Juno measurement of the asymmetric gravity field (for $J_3 - J_9$) as function of latitude and the corresponding values from the best-fit solution (panels a and b), showing a good match between the measurement and the optimized solution (see calculation in Methods).

$\times 10^{-8}$	Measured	Model without latitudinal variation	Model with latitudinal variation
J_3	-4.24 ± 0.97	-5.71 ± 1.67	-5.96 ± 2.33
J_5	-6.89 ± 0.81	-7.73 ± 0.41	-8.00 ± 0.43
J_7	12.39 ± 1.68	12.77 ± 0.54	12.04 ± 0.70
J_9	-10.58 ± 4.35	-8.84 ± 0.42	-9.71 ± 0.72

Table 1: **The Juno measured and model odd gravity harmonics**. Model results are shown for both optimizations with and without variation of flow depth with latitude. The uncertainty is the 3σ uncertainty values. The model uncertainty is calculated by the optimization procedure (Methods). For the middle (right) column the J_n values correspond to the parameter values given in the caption of Fig. 3 (Fig. 4).

Methods

Calculation of the dynamical gravity harmonics. The gravity harmonics (J_n) are defined as a weighted integral over the interior density distribution $J_n = -(Ma^n)^{-1} \int P_n \rho r^n d^3 \mathbf{r}$, where M is the planetary mass, a is the equatorial radius, P_n is the n-th Legendre polynomial, ρ is the local density and r is the local radius[31]. On planets with internal dynamics, the density is perturbed by the flow so that the total density in J_n can be written as $\rho = \rho_s + \rho'$, where the density ρ_s is the hydrostatic density resulting from the background rotation and internal density distribution[32,33,34,28,35], and ρ' are the density fluctuations arising from atmospheric and internal dynamics[20]. The gravity harmonics can be similarly decomposed into two parts $J_n = J_n^s + \Delta J_n$, where the static component (J_n^s) is due to the planet's internal density distribution and shape[13,36], and the dynamical component (ΔJ_n) is due to the density deviations related to the flow[20].

In order to develop the relation between the flow on Jupiter and the gravity field measured by Juno, we consider the full momentum balance on a rotating planet

$$\frac{\partial \mathbf{u}}{\partial t} + (\mathbf{u} \cdot \nabla)\mathbf{u} + 2\Omega \times \mathbf{u} + \Omega \times \Omega \times \mathbf{r} = -\frac{1}{\rho}\nabla p + \nabla \Phi, \tag{M1}$$

where $\mathbf{u}$ is the 3D flow vector, Ω is the planetary rotation rate (1.76×10^{-4} s^{-1}), ρ is density, p is pressure and Φ is the body force potential set by gravity so that $\nabla \Phi = -\mathbf{g}$[37]. The first term on the left hand side is the local acceleration of the flow, the second is the Eulerian advection, the third is the Coriolis acceleration, and the fourth is the centrifugal acceleration. On the right hand side appear the pressure gradient and the body force. Frictional forces are neglected. For Jupiter parameters, and large scale motion, the Rossby number is small $Ro \equiv U/\Omega L \approx 0.05$, where U is the typical value of the velocity O(100 m s^{-1}), and L is the typical jet scale O(10^4 km). The small Rossby number implies that the first two terms are negligible compared to the Coriolis term, so that

$$2\Omega \times (\rho \mathbf{u}) = -\nabla p - \rho \mathbf{g} - \rho \Omega \times \Omega \times \mathbf{r}. \tag{M2}$$

Since for Jupiter parameters the ratio between the two latter terms on the right hand side of Eq. (M2), is $\frac{a\Omega^2}{g} \approx 0.1$, and not two orders of magnitude smaller as it is for Earth parameters, we do not appriori make the traditional approximation merging the centrifugal force with the gravity term[38], but solve for the full system, allowing the density, pressure and gravity to be functions of radius (r) and latitude (θ). We separate the

solution to a static solution in which $\mathbf{u} = 0$, and $\rho_s(r, \theta)$, $p_s(r, \theta)$, and $\mathbf{g}_s(r, \theta)$ are solutions to the leading order equation

$$0 \ = \ -\nabla p_s - \rho_s g_s - \rho_s \Omega \times \Omega \times \mathbf{r}, \tag{M3}$$

and a deviation due to the dynamics $\rho'(r, \theta)$, $p'(r, \theta)$, and $\mathbf{g}'(r, \theta)$, where $\rho = \rho_s + \rho'$, $p = p_s + p'$ and $\mathbf{g} = \mathbf{g}_s + \mathbf{g}'$. For the static part of the solution we use solutions from internal models[39,28]. Subtracting Eq. (M3) from Eq. (M2) gives the leading order dynamical equation

$$2\Omega \times (\rho_s \mathbf{u}) = \ -\nabla p' - \rho_s \mathbf{g}' - \rho' \mathbf{g}_s - \rho' \Omega \times \Omega \times \mathbf{r}. \tag{M4}$$

Taking the curl of Eq. M4, eliminating the dependence on pressure, yields a single equation in the azimuthal direction

$$-2\Omega r \partial_z (\rho_s u) \ = \ -r g_s^{(\theta)} \frac{\partial \rho'}{\partial r} - g_s^{(r)} \frac{\partial \rho'}{\partial \theta} + r \frac{\partial \rho_s}{\partial r} g'^{(\theta)} - g'^{(r)} \frac{\partial \rho_s}{\partial \theta} - \Omega^2 r \left[\frac{\partial \rho'}{\partial \theta} \cos^2 \theta + \frac{\partial \rho'}{\partial r} r \cos \theta \sin \theta \right] \tag{M5}$$

where u is the velocity component in the azimuthal direction, and the notation $\partial_z \equiv \cos \theta \frac{1}{r} \frac{\partial}{\partial \theta} + \sin \theta \frac{\partial}{\partial r}$ denotes the derivative along the direction of the axis of rotation. Note that this is an integro-differential equation since both the gravity $\mathbf{g}_s$ and $\mathbf{g}'$, are calculated by integrating ρ_s and ρ', respectively. Although this equation can be solved numerically[18], it is very difficult to solve at the required resolution and the approximation below is sufficient for relating the flow field and the gravity harmonics[18].

A typical solution to Eq. M5, corresponding to the flow field in Fig. 3 in the main text, is given in Fig. ED1. It shows that the leading order balance is between the left hand side term and the second term on the right hand side of Eq. M5. All other terms are at least an order of magnitude smaller, and have a very small contribution to the gravitational harmonics[18]. Thus, taking $g = g_s(r)$ in Eq. M4 and neglecting the centrifugal term gives the leading order solution. Taking the curl of Eq. M4 gives then the leading order equation

$$2\Omega \cdot \nabla (\rho_s \mathbf{u}) = \nabla \rho' \times \mathbf{g}, \tag{M6}$$

which is Eq. 1 in the main text, and is a form of the thermal wind equation[15,20]. Note that if a higher correction is desired, all terms in Eq. M5 must be maintained since the smaller terms in Eq. M5 partially cancel each other (Fig. ED1). Approximations not maintaining all these terms would be invalid[16].

20

45   The zonal component of Eq. M6 is then

$$2\Omega r \partial_z (\rho_s u) \quad = \quad g_s^{(r)} \frac{\partial \rho'}{\partial \theta}, \tag{M7}$$

46   which can be integrated to find a solution for the dynamical part of the density given by

$$\rho'(r,\theta) \quad = \frac{2\Omega r}{g_s} \quad \int^{\theta} \partial_z \left(\rho_s(r) u(r,\theta') \right) d\theta' + \rho'_0(r), \tag{M8}$$

47   where $\rho'_0(r)$ is an unknown integration function that depends only on radius. Although the density ρ' can not

48   be determined uniquely due to the unknown $\rho'_0(r)$, the gravity harmonics due to dynamics

$$\Delta J_n = -\frac{2\pi}{Ma^n} \int\limits_{-\pi/2}^{\pi/2} \cos\theta d\theta \int\limits_{0}^{a} r^{n+2} P_n (\sin\theta) \rho'(r,\theta) dr, \tag{M9}$$

49   can be determined uniquely since

$$\int\limits_{-\pi/2}^{\pi/2} \cos\theta d\theta \int\limits_{0}^{a} r^{n+2} P_n (\sin\theta) \rho'_0(r) dr = 0. \tag{M10}$$

50   To avoid integrating over discontinuities at the equator the integration is performed from the equator poleward

51   in both hemispheres separately[40]. Therefore, given any flow profile, the anomalous density gradient can

52   be determined to leading order (Eq. M8) and the resulting dynamical gravity harmonics can be calculated

53   (Eq. M9). Note that the sphericity assumption leaves the choice of using the equatorial radius or the mean

54   radius. For consistency with the standard normalization[41,5] of J_n we use the equatorial radius, but repeating

55   the calculation with the mean radius gives results within one percent of those presented here.

56

57   **Calculation of the gravity anomaly.** Equivalent to the gravity harmonics is the physical gravity anomaly

58   (Fig. 4c), which emphasizes the nature of the solution as function of latitude[20]. The gravity anomaly in the

59   radial direction on the surface of a planet that results from the asymmetric flow is given by

$$\Delta g_r(\theta) \quad = \quad -\frac{GM}{a^2} \sum_n (n+1) \Delta J_n P_n (\sin\theta), \tag{M11}$$

60   with $n = 3,5,7,9$. In Fig. 4c in the main text we show a comparison between the measured[5] and the calculated

21

61   gravity anomalies. The better match at low latitudes is a result of the measurements having smaller uncertain-

62   ties at low latitudes due to the trajectory of the spacecraft being at periapses near Jupiter's lower latitudes

63   during the initial phase of the Juno mission [12,41].

64

65   **Setup of the flow structure.** Knowledge of the flow field of Jupiter to date comes almost completely

66   from cloud tracking [42,11]. We use this flow field as an upper boundary, and extend the flow into the interior by

67   optimizing the general functions below. Angular momentum constraints require that the flow into the interior

68   follows angular momentum surfaces [26,15,19] (see discussion in the main text), which on Jupiter are nearly

69   parallel to the direction of the axis of rotation. Magnetic drag [7] and the compressibility of the fluid [15] require

70   that the flow decays at some depth, and therefore we use a flow field with the following general structure

$$u(r,\theta) \quad = \quad u_{\mathrm{cyl}}(s)Q(r), \tag{M12}$$

71   where $u_{\mathrm{cyl}}(s)$ is the cloud-level azimuthal wind projected downward along the direction of the axis of rotation,

72   and $s = r\cos(\theta)$ is the distance from the axis of rotation. $Q(r)$ is the radial decay function we optimize, given

73   by

$$Q(r) \quad = \quad (1-\alpha)\exp\left(\frac{r-a}{H(\theta)}\right) + \alpha\left[\frac{\tanh\left(-\frac{a-H(\theta)-r}{\Delta H}\right)+1}{\tanh\left(\frac{H(\theta)}{\Delta H}\right)+1}\right], \tag{M13}$$

74   where a is the planetary radius, α is the contribution ratio between an exponential and a normalized hyperbolic

75   tangent function and ΔH is the width of the hyperbolic tangent. We take a hierarchal approach using this profile

76   at several levels of complexity. First, setting $\alpha = 0$, the flow is parameterized as a simple exponential decay,

77   with H being independent of latitude, as has been done in many previous studies [20,6,43,44,10]. Then, allowing

78   $0 < \alpha < 1$, the flow is parameterized (Fig. 3 of the main text), with three free parameters, α, H and ΔH as

79   they appear in Eq. M13, but still keeping H as a single number. As a final step (Fig. 4 of the main text), H is

80   allowed to vary as a function of latitude and defined as

$$H(\theta) = H_0 + H_2 P_2(\sin\theta), \tag{M14}$$

81   where H_0 is the single latitude independent depth used in the first and second setups, and H_2 is the additional

82   parameter used to set the amplitude of the latitude dependent second Legendre polynomial function P_2. For

22

the optimization shown in Fig. 4 in the main text the values are $H_0 = 1619 \pm 150$ and $H_2 = -1519 \pm 459$. Note that the hyperbolic function is normalized by its value at the surface of the planet to assure that the surface flow has the value of the measured cloud-level wind. Expansion of $H(\theta)$ to higher harmonics is possible, but additional optimized parameters increase the solution uncertainty (see below), and therefore we restrict this expansion only to second order.

The Optimization procedure. The methodology described here is similar to that used in Galanti and Kaspi (2017)[24]. We find the values of a set of control variables that bring the model solution for the gravity harmonics to be as close as possible to the measured gravity harmonics. The number of optimized control variables in the three setups varies between one and four parameters as discussed above. The measure for the desired proximity of the model solution to the measurements (a cost-function) takes into account our knowledge regarding the observational errors. The optimization procedure provides an efficient way to reach the global minimum of the cost-function.

Since α has different units than H and ΔH, the problem is best conditioned when the total control vector is composed from the different parameters normalized by their typical values. We define the general control vector as

$$\overrightarrow{\mathbf{X_C}} = \{H_0/h_{\mathrm{nor}}, \Delta H/h_{\mathrm{nor}}, \alpha/\alpha_{\mathrm{nor}}, H_2/h_{\mathrm{nor}}\}, \tag{M15}$$

where $h_{\mathrm{nor}} = 10^7$ m and $\alpha_{\mathrm{nor}} = 1$. In the optimization procedure, the values of the normalized control variables $H_0/h_{\mathrm{nor}}, \alpha/\alpha_{\mathrm{nor}}$, and $\Delta H/h_{\mathrm{nor}}$ are limited to the range of 0 to 1, and the value of H_2/h_{nor} between -1 and 1.

The cost-function is defined as the weighted difference between the model calculated odd harmonics and those measured by Juno. Together with an additional penalty term to ensure that initial guess does not affect the solution, the cost-function is

$$L = (\mathbf{J^m} - \mathbf{J^o})^{\mathbf{T}} \mathbf{W} (\mathbf{J^m} - \mathbf{J^o}) + \varepsilon \mathbf{X_C^T} \mathbf{X_C}, \tag{M16}$$

where $\mathbf{J^m} = \{J_3^{\mathrm{m}}, J_5^{\mathrm{m}}, J_7^{\mathrm{m}}, J_9^{\mathrm{m}}\}$ is the calculated model solution , $\mathbf{J^o} = \{J_3^{\mathrm{o}}, J_5^{\mathrm{o}}, J_7^{\mathrm{o}}, J_9^{\mathrm{o}}\}$ is the measured one, and $\mathbf{W}$ is 4×4 weight matrix (Table ED2) calculated as the inverse of the covariance matrix multiplied by 9 (equivalent to 3 times the uncertainties). The diagonal terms give the weight assigned to each harmonic independently, and the off-diagonal terms give the weights resulting for the cross correlation of the measure-

ment errors. The larger the value, the more weight is given in the cost-function. For example, looking at the diagonal terms, the largest weight is given to J_5 and the smallest one to J_9. Importantly, the off diagonal terms have values that are as large as the diagonal terms, i.e., there is a strong correlation between the measurement errors, and therefore we demand that the discrepancy between the model harmonics and the measured ones will also be cross correlated in the same manner. The second term in Eq. M16 acts as a penalty term (also known as 'regularization') whose purpose in this case is to ensure that the optimized solution is not affected by the initial guess, or any part of the control vector that does not affect the difference between the calculated and observed gravity harmonics. An extensive discussion of this issue (also known as the null space of the solution) can be found in previous studies [18,24]. The value of the parameter ε is set according to the initial value of the cost-function, so it affects the solution only when the cost-function is reduced considerably. The form of the penalty term is set to penalize any non-zero value of the control variable $\mathbf{X_C}$ since there is no prior knowledge of the depth of the flow. Given an initial guess for $\overrightarrow{\mathbf{X}_C}$, a minimal value of L is searched for using the Matlab function 'fmincon' and taking advantage of the cost-function gradient that is calculated with the adjoint of the dynamical model [9].

Calculating the uncertainties in the solution. The control variable uncertainties are derived from the Hessian matrix $\mathbf{G}$ (second derivative of the cost-function L with respect to the control vector $\mathbf{X_C}$)[9]. For example, in the third setup of the optimization there are 4 parameters that are optimized, therefore the size of the Hessian matrix will be 4×4. Inverting the Hessian matrix $\mathbf{G}$, we get the solution error covariance matrix $\mathbf{C}$. This matrix includes the error covariance associated with combination of each two control variables (off diagonal terms), and the variance of each one (diagonal terms). Physically, the covariance matrix indicates to the formal uncertainties in the control variables given the uncertainties of the observations (weights $\mathbf{W}$ in the cost-function). The larger the uncertainties in the observations, the smaller are the weights in the cost-function, and the larger the uncertainties in the control variables. The uncertainties appearing in this study for H, ΔH, and α, are the square root of the diagonal terms in the matrix $\mathbf{C}$. Note that in all cases analyzed in this work, the off-diagonal terms in $\mathbf{C}$ have the same order of magnitude as the diagonal terms, meaning that uncertainties in the control variable are highly correlated.

Using the uncertainties in the control variable, we can calculate the uncertainties in the model solution for J_n. Since the uncertainties for H, ΔH, and α represent the 1$^{\text{st}}$ standard deviation of the errors, we can statistically estimate the associated error in the J_n by solving the model with the parameters randomly perturbed

24

around their optimized value (with the perturbations having a normal distribution with the calculated standard deviation). In this study we generate 1000 such cases, calculate the J_n for each case, and then calculate the standard deviation for each J_n. This is the error value given to each gravity harmonic in Table 1 of the main text, and Table ED1.

Statistical significance test for the latitudinal profile. One of the conclusions of the manuscript is that the observed cloud-level meridional wind profile, as observed at the cloud-level, extends deep into the interior. This is a strong constraint on the flow, which we investigate its statistical significance here. Since we are optimizing a solution with only four measurements, there exists a possibility that the match obtained with the gravity measurements is by chance and not because the same meridional profile extends to great depths. In order to exclude this possibility we examine whether a match with the gravity measurements could be obtained when using a different meridional wind profile than that of the cloud-level flows. To make a sensible test the artificial wind profile we examine should have similar characteristics, such as the typical latitudinal width of the jets and their amplitude. To accomplish this, the observed cloud-level wind is decomposed into the first 100 Legendre polynomials

$$U_{\text{surf}}(\theta) \quad = \quad \sum_{i=0}^{99} A_i P_i(\sin\theta), \tag{M17}$$

where A_i are the coefficients of the Legendre polynomials. To create the different artificial wind possibilities, the wind is then reconstructed as

$$U_{\text{rand}}^j(\theta) \quad = \quad \sum_{i=0}^{99} S_i^j A_i P_i(\sin\theta), \tag{M18}$$

where S_i^j are a 100 plus or minus signs randomly chosen for each realization j of the wind. The resulting artificial cloud-level wind retains the basic characteristics (width and strength) of the observed zonal jets, but their latitudinal locations are now very different. In order to statistically examine our ability to reach a solution that gives a good match between the model calculated gravity harmonics and those measured, 1000 artificial cloud-level wind profiles were generated. Few examples of such randomly generated winds are shown in Fig. ED3. Note that while the wind profiles are very different one from the other, the main

25

characteristics of the observed winds are kept. Fig. ED4 shows the resulting J_3, J_5, J_7 and J_9 for these flow profiles (blue dots), optimized in the same way that the cloud-level winds are. The results indicate that the gravity harmonics calculated using the specific cloud-level wind profile (black points with their uncertainty ellipse), give results closer to the measurements (red points with their uncertainty ellipse) than 99% of the random profiles, indicating the robustness of this result. Note the tendency of the optimized solutions to be in the quarter of the phase space where the measurements are (Fig. ED4), particularly for the case of J_5 and J_7, because for these harmonics the absolute value of the measurement is largest and the relative measurement error is smallest (see Table 1 in the main text), so their weight in the cost-function is the largest. Taking the same random set of meridional profiles and calculating their gravity harmonics for a fixed vertical profile (without the optimization process), gives solutions spread equally over all quarters of the parameter space (Fig. ED5). This illustrates that also the tendency of the simple exponential decay solution to have the correct sign and magnitude (Fig. 2 in the main text) is very likely not by chance. As an additional test we calculate the solution taking the Jupiter observed cloud-level meridional profile, but extended into the interior radially instead of along the direction of the spin axis. In this case even the sign of the gravity harmonics differs from the measurements.

Non-uniqueness of the gravity inversion. It is important to note that the gravity inversion problem is non-unique, and as demonstrated in Figs. 3 and 4 different profiles can give similar gravity signatures. In addition, the cases presented here do not match the measurements perfectly, and with more free parameters and/or other meridional profiles[45] one could achieve better matches to the measurements. However, since the problem is non-unique, achieving a perfect match is not necessarily meaningful. Thus, the rational of this study is to show that using a minimal set of assumptions about the vertical and meridional structure, gives by itself a very good, and statistically significant, match to the measurements, indicating the structure and extent of the flow. Regardless of the exact vertical profile (which can depend on the parameterization and the non-uniqueness) the gravity measurements robustly reveal that the east-west jet-streams on Jupiter are very deep, reaching several thousands of kilometers beneath the cloud-level (several tens of kbar in pressure), and advect a significant mass that is on the order of 1% the mass of the planet.

Code availability: code for inversion of the gravity data is available at:

http://www.weizmann.ac.il/eserpages/kaspi/juno_code/

References

31. Hubbard, W. B. *Planetary Interiors* (pp. 343. New York, Van Nostrand Reinhold Co., 1984).

32. Guillot, T. & Morel, P. CEPAM: a code for modeling the interiors of giant planets. *Astron, and Astro, Supp. ser.* **109**, 109–123 (1995).

33. Militzer, B., Soubiran, F., Wahl, S. M. & Hubbard, W. B. Understanding Jupiter's interior. *J. Geophys. Res. (Planets)* **121**, 1552–1572 (2016).

34. Miguel, Y., Guillot, T. & Fayon, L. Jupiter internal structure: the effect of different equations of state. *Astron. and Astrophys.* **596**, A114 (2016).

35. Helled, R. & Stevenson, D. J. The fuzziness of giant planets' cores. *Astrophys. J. Let.* **840**, L4 (2017).

36. Wisdom, J. & Hubbard, W. B. Differential rotation in Jupiter: A comparison of methods. *Icarus* **267**, 315–322 (2016).

37. Pedlosky, J. *Geophysical Fluid Dynamics* (pp. 710. Springer-Verlag, 1987).

38. Vallis, G. K. *Atmospheric and Oceanic Fluid Dynamics* (pp. 770. Cambridge University Press., 2006).

39. Hubbard, W. B. Conventric maclaurin spheroid models of rotating liquid planets. *Astrophys. J.* **768** (2013).

40. Kong, D., Zhang, K. & Schubert, G. Odd gravitational harmonics of Jupiter: Effects of spherical versus nonspherical geometry and mathematical smoothing of the equatorially antisymmetric zonal winds across the equatorial plane. *Icarus* **277**, 416–423 (2016).

41. Folkner, W., Iess, L., Tortora, P. & more. Jupiter gravity field from first two orbits by Juno. *Geophys. Res. Lett.* **44**, 4694–4700 (2017).

42. Porco, C. C. *et al.* Cassini imaging of Jupiter's atmosphere, satellites and rings. *Science* **299**, 1541–1547 (2003).

43. Kaspi, Y., Showman, A. P., Hubbard, W. B., Aharonson, O. & Helled, R. Atmospheric confinement of jet-streams on Uranus and Neptune. *Nature* **497**, 344–347 (2013).

44. Kong, D., Zhang, K. & Schubert, G. Wind-induced odd gravitational harmonics of Jupiter. *Mon. Not. Roy. Astro. Soc.* **450**, L11–L15 (2015).

45. Dowling, T. E. Estimate of Jupiter's deep zonal-wind profile from Shoemaker-Levy 9 data and Arnold's second stability criterion. *Icarus* **117**, 439–442 (1995).
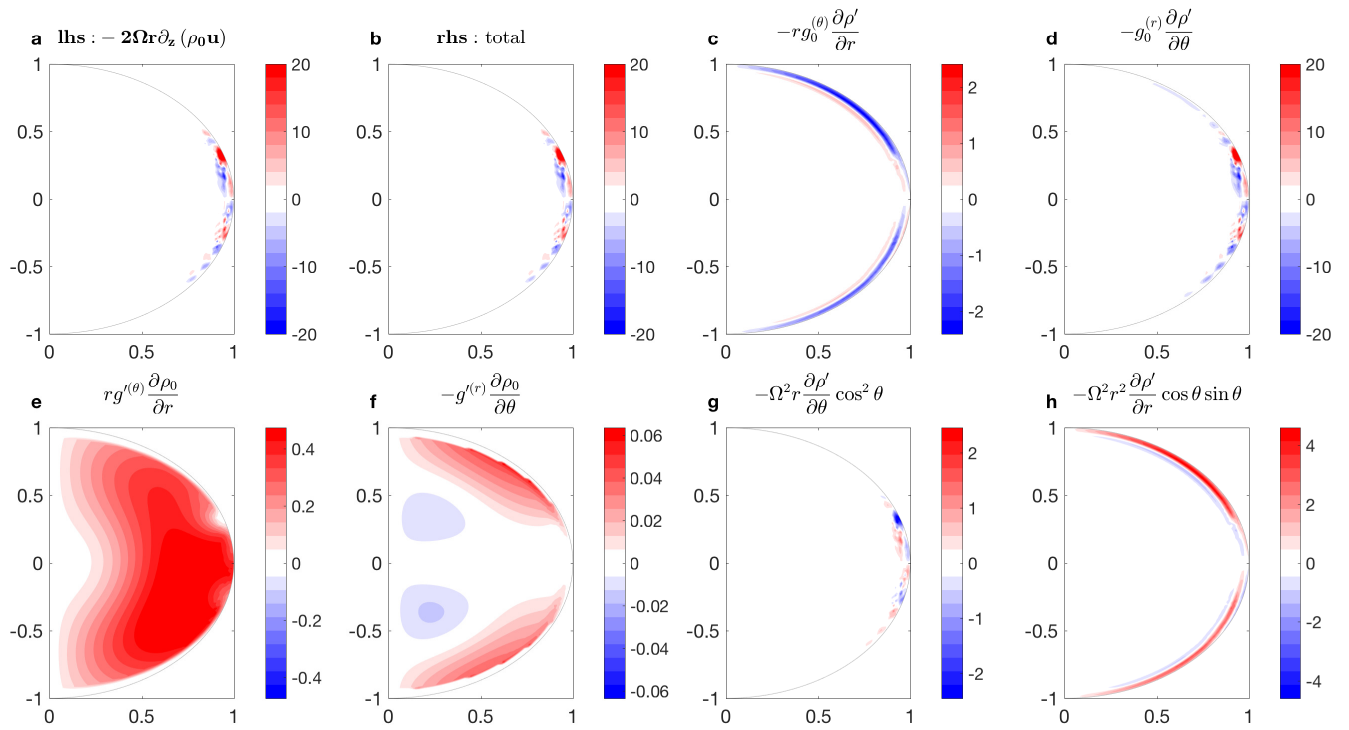
Extended Data Figures

Figure ED1: **The vorticity balance.** Solution to Eq. M5 **a.** left hand side term with the wind profile from Fig. 3 in the main text, **b.** total of the right hand side, **c-h.** the six terms on the right hand side of Eq. M5, showing that the thermal wind balance (panels a and d) is the leading order balance. Note that the different panels have different color scales.
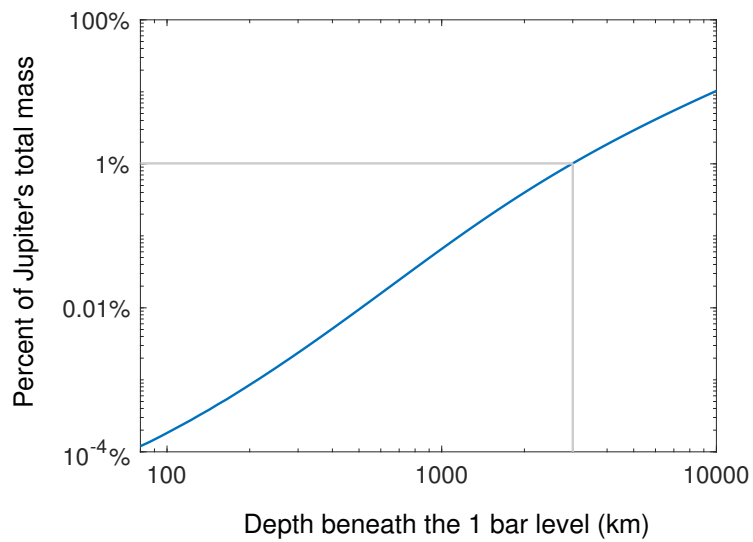
Figure ED2: **Jupiter's mass distribution.** The percent of Jupiter's mass as function of depth beneath the 1-bar level. The gray line shows that roughly 1% of the mass is contained above a depth of 3000 km.
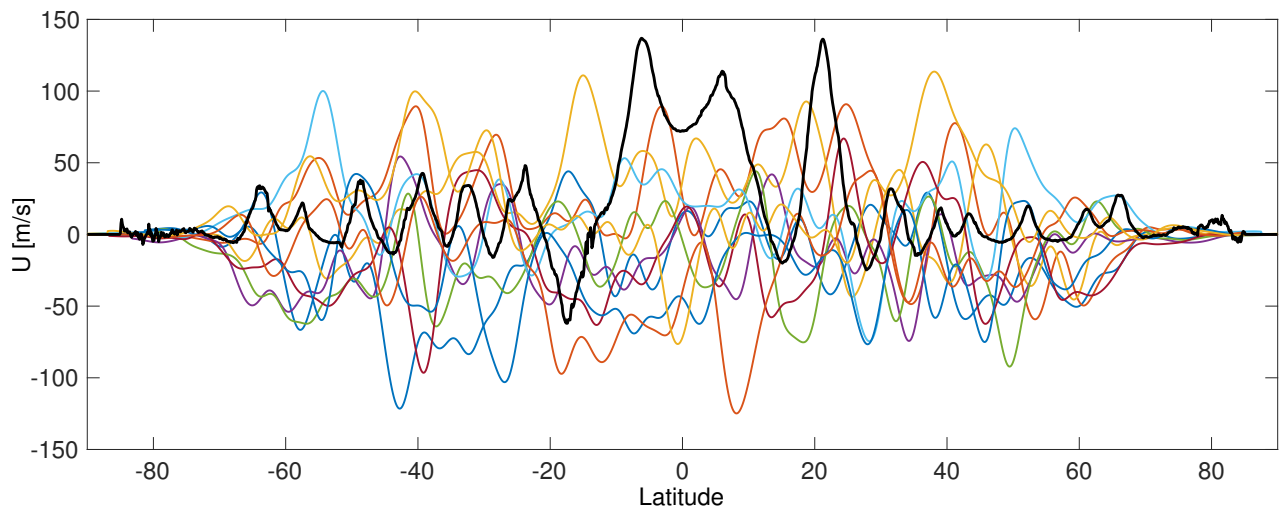
Figure ED3: **Example of wind profiles used for the statistical significance test.** The observed cloud-level wind (black), together with a sample of 10 randomly generated wind profiles.
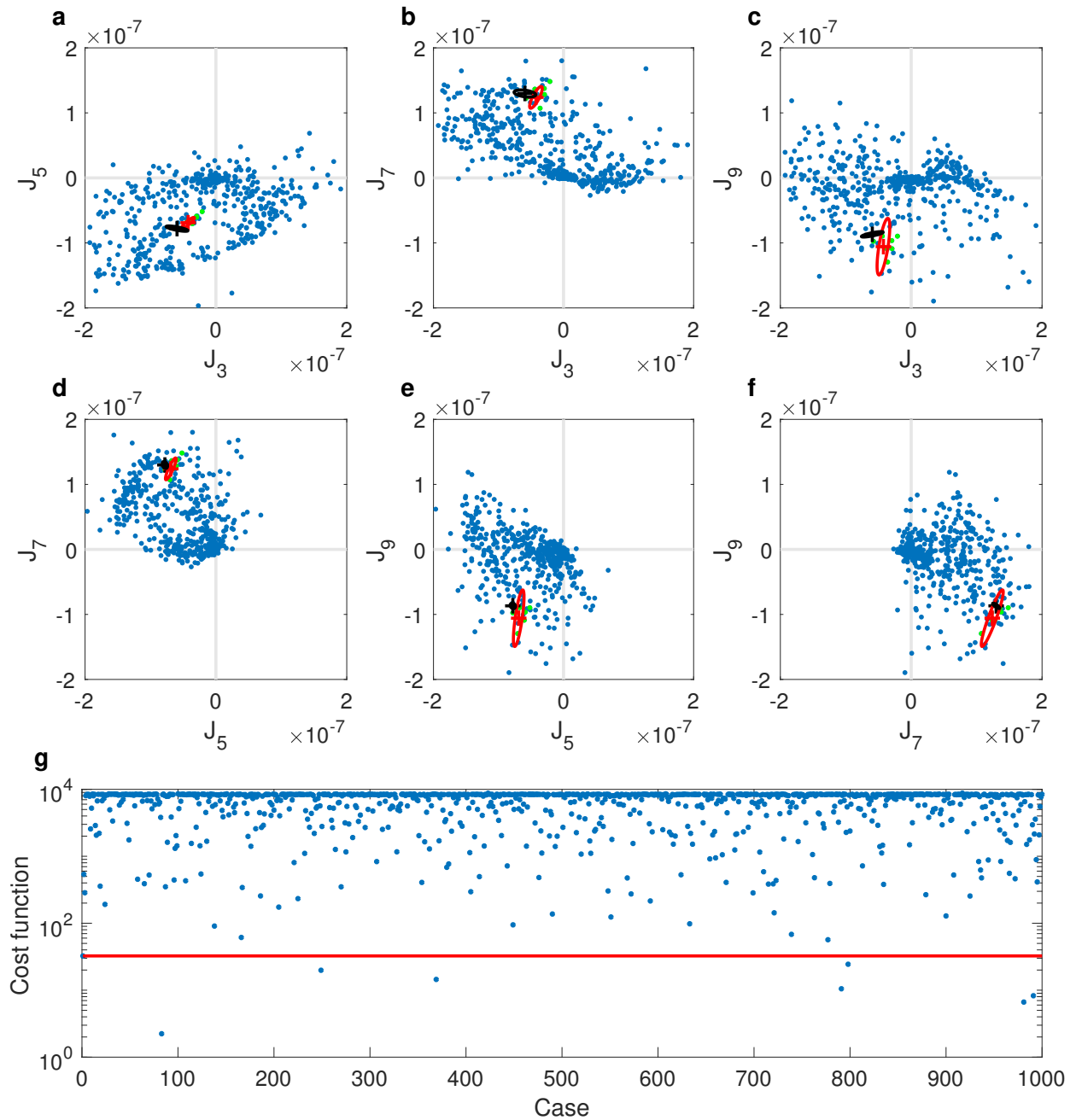
Figure ED4: **Optimized solutions for the odd harmonics using random meridional wind profiles. a-f.** Optimized solutions (blue) for J_3, J_5, J_7 and J_9 for flows with 1000 different artificial meridional profiles (as in Fig. ED3). The Juno measurements are shown in red with their corresponding uncertainty ellipse. The optimized solution corresponding to Jupiter's observed cloud-level meridional wind profile (Fig. 3 in the main text) is shown in black with the corresponding uncertainty ellipse. **g.** The cost-function for all different meridional profiles explored, with the red line corresponding to the solution with the Jupiter meridional wind profile. Less than 1% of the solutions have lower cost functions (green dots in panels a-f).
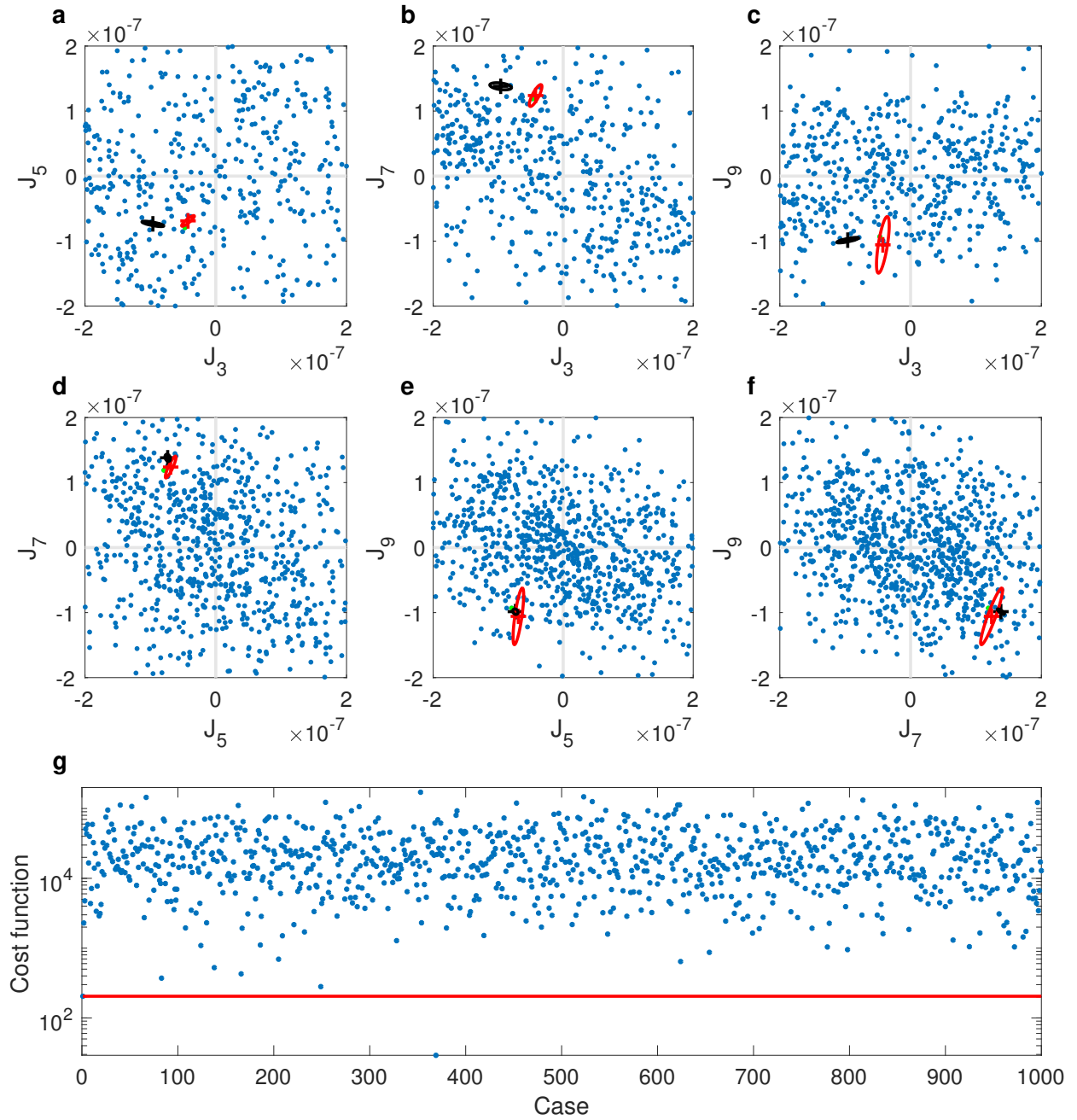
Figure ED5: **Solutions for the odd harmonics using random meridional wind profiles and a fixed vertical profile. a-f.** Solutions (blue) for J_3, J_5, J_7 and J_9 for flows with 1000 different artificial meridional profiles (as in Fig. ED3), and the vertical profile held fixed with $H = 2000$ km, $\Delta H = 1500$ km and $\alpha = 1$. The Juno measurements are shown in red with their corresponding uncertainty ellipse. The solution with these parameters and using Jupiter's observed cloud-level meridional wind profile is shown in black with the corresponding uncertainty ellipse. **g.** The cost-function for all different meridional profiles explored, with the red line corresponding to the solution with the Jupiter meridional wind profile. This shows that when no optimization is done (which takes into consideration the relative measurement error of the different harmonics), the solutions are spread equally over all four quadrants in these phase spaces (different than Fig. ED4).

$\times 10^{-8}$	Model without latitudinal variation	Model with latitudinal variation
ΔJ_2	54.62 ± 5.21	-48.87 ± 7.93
ΔJ_4	-5.18 ± 0.74	-15.01 ± 7.56
ΔJ_6	0.33 ± 0.35	0.29 ± 1.49
ΔJ_8	5.41 ± 0.28	4.76 ± 0.61
ΔJ_{10}	-5.35 ± 0.25	-4.94 ± 0.71

Table ED1: **The flow induced even gravity harmonics corresponding to the optimized solutions in Table 1.** The even gravity harmonics solutions for the optimization, with and without variation of flow depth with latitude, that correspond to the solutions presented in Figs. 3 and 5 and Table 1 of the main text. The uncertainties are the 3σ uncertainty values.

	J_3	J_5	J_7	J_9
J_3	8.32	-11.05	1.45	-0. 41
J_5	-11.05	20.21	-12.26	3.35
J_7	1.45	-12.26	14.31	-7.63
J_9	-0. 41	3.35	-7.63	7.91

Table ED2: **The weights matrix W used in the cost function L (Eq. M16).** Shown are the weights associated with J_3, J_5, J_7 and J_9 (diagonal terms) and those associated with the correlation between the harmonics (off-diagonal terms). The values reflect the uncertainties in the measurements, calculated taking the inverse of the measurement error covariance matrix multiplied by 9 (to reflect 3σ uncertainties). The larger the value, the larger the weight given to it when minimizing the cost-function. Values shown are multiplied by 10^{-16}.